LOCKHEED MARTIN ENERGY RESEARCH LIBRARIES
3 4456 0451475 5

CENTRAL RESEARCH LIBRARY
DOCUMENT COLLECTION

2

ORNL-3702
UC-34 – Physics
TID-4500 (37th ed.)

A NEW TECHNIQUE FOR MEASURING RANGE OF LOW ENERGY CHARGED PARTICLES IN CONDUCTING SOLIDS

(THESIS)

A. K. Roecklein
M. Y. Nakai
E. T. Arakawa
J. L. Stanford
R. D. Birkhoff

OAK RIDGE NATIONAL LABORATORY
operated by
UNION CARBIDE CORPORATION
for the
U.S. ATOMIC ENERGY COMMISSION

CENTRAL RESEARCH LIBRARY
DOCUMENT COLLECTION
LIBRARY LOAN COPY
DO NOT TRANSFER TO ANOTHER PERSON
If you wish someone else to see this document, send in name with document and the library will arrange a loan.

Printed in USA. Price $3.00. Available from the Clearinghouse for Federal Scientific and Technical Information, National Bureau of Standards, U.S. Department of Commerce, Springfield, Virginia

LEGAL NOTICE

This report was prepared as an account of Government sponsored work. Neither the United States, nor the Commission, nor any person acting on behalf of the Commission:

A. Makes any warranty or representation, expressed or implied, with respect to the accuracy, completeness, or usefulness of the information contained in this report, or that the use of any information, apparatus, method, or process disclosed in this report may not infringe privately owned rights; or

B. Assumes any liabilities with respect to the use of, or for damages resulting from the use of any information, apparatus, method, or process disclosed in this report.

As used in the above, "person acting on behalf of the Commission" includes any employee or contractor of the Commission, or employee of such contractor, to the extent that such employee or contractor of the Commission, or employee of such contractor prepares, disseminates, or provides access to, any information pursuant to his employment or contract with the Commission, or his employment with such contractor.

ORNL-3702

Contract No. W-7405-eng-26

HEALTH PHYSICS DIVISION

A NEW TECHNIQUE FOR MEASURING RANGE OF LOW ENERGY CHARGED PARTICLES IN CONDUCTING SOLIDS

A. K. Roecklein
M. Y. Nakai
E. T. Arakawa
J. L. Stanford
R. D. Birkhoff

Submitted as a thesis to the Graduate School of Vanderbilt University in partial fulfillment of the requirements for the degree of Master of Science

MARCH 1965

OAK RIDGE NATIONAL LABORATORY
Oak Ridge, Tennessee
operated by
UNION CARBIDE CORPORATION
for the
U.S. ATOMIC ENERGY COMMISSION

LOCKHEED MARTIN ENERGY RESEARCH LIBRARIES

3 4456 0451475 5

ACKNOWLEDGMENTS

The authors take great pleasure in expressing sincere appreciation to L. C. Emerson for advice on optical interferometric method for thin film thickness measurement and to J. A. Harter and D. Pittman for their assistance on electronic problems arising during this work.

This research was partially supported by the Atomic Energy Commission through its Special Fellowship Program in Health Physics which is administered by the Oak Ridge Institute of Nuclear Studies. Experimental work was conducted in the facilities of the Health Physics Division at Oak Ridge National Laboratory.

TABLE OF CONTENTS

Page

ACKNOWLEDGMENTS ii

LIST OF FIGURES iv

LIST OF TABLES v

I. INTRODUCTION 1

II. THEORY 7

A. Lindhard-Scharff Stopping Power Theory for Heavy Particles 7
B. Analysis of Current-Energy Curves and Definition of Range of Charge 11

III. EXPERIMENTAL APPARATUS AND PROCEDURE 14

A. Radio-Frequency Ion Source 14
B. Accelerator, Expulsion and Focus Anode Circuit, and Procedure for Beam Energy Analysis 18
C. Collimator and Secondary Electron Bias Plate . 21
D. Target Foil Design and Evaporating Apparatus . 24
E. Current and Resistance Measuring Circuits and Procedure for Resistance Regeneration 27
F. Optical Interferometer for Thickness Measurement 31
G. Thin Film Thickness Monitor 34
H. Silicon Monoxide Thickness Determination by Neutron Activation 35

IV. DATA 37

V. RESULTS 43

VI. REVIEW AND CONCLUSIONS 46

BIBLIOGRAPHY 47

LIST OF FIGURES

Figure — Page

1. Cross-sectional View of Evaporated Target (Not to Scale) ... 6
2. Photograph of Experimental Apparatus 15
3. Diagram of R-F Ion Source and Oscillator Circuit 16
4. Schematic Diagram of Experimental Apparatus 17
5. Schematic Diagram of Apparatus for Measurement of Energy Distribution in Beam 20
6. Collector Current versus Stopping Potential for Measurement of Beam Energy Distribution 22
7. Collector Current versus Collimator Voltage for Suppression of Secondary Electron Emission from Collector 23
8. Photograph of Evaporated Target 25
9. Diagram of Evaporating Source for Aluminum 26
10. Diagram of Evaporating Source for Silicon Monoxide 28
11. Target Current and Resistance Measuring Circuit 29
12. Schematic Diagram of Optical Interferometer 33
13. Photograph of Fringe Shift for an Aluminum Foil, 475 Å Thick. 33
14. Fractional Current Distribution in the Aluminum Layers versus Proton Energy for Aluminum Thicknesses
    a. 200 Å 38
    b. 350 Å 39
    c. 1,050 Å 40
15. Proton Transmission as a Function of Energy for Several Aluminum Thicknesses 41
16. Aluminum Thickness as a Function of Energy for 50% Proton Transmission 42
17. Comparison of Theoretical and Experimental Range-Energy Curves 44

LIST OF TABLES

Table | Page

I. Previous Experimental Work on Low Energy Charged Particle Absorption 3

ABSTRACT

A new method is described for measuring ranges of charged particles in conducting solids, and experimental data are presented for proton ranges in aluminum at energies less than 10 keV. A thickness of aluminum which is greater than the maximum range of protons at this energy, is evaporated onto a glass substrate in a system evacuated to 1.0×10^{-5} mm Hg. This layer is covered by an extremely thin (≤ 75 Å) layer of silicon monoxide which is a good electrical insulator. The thickness of the SiO layer was determined both by a neutron-activation-beta-counting procedure and by using a quartz-oscillator, film-thickness monitor during evaporation. A second aluminum layer was then evaporated onto the SiO layer and its thickness was accurately measured by optical interferometry. The two aluminum layers were separated by an electrical resistance across the SiO layer of the order of 1 megohm and each was provided with current leads to a galvanometer.

The proton beam was extracted from a radio-frequency ion source and accelerated to the desired energy by a series of anodes in an evacuated system. An electrostatic stopping potential analysis was performed to determine the energy distribution in the beam. Protons were incident normally on the top aluminum layer and fractional currents to the top and bottom aluminum layers were measured as the beam energy was increased. Curves for proton transmission as a function of energy were derived from the normalized current data for several aluminum film thicknesses. The energy at which 50% of the current protons were transmitted was determined for several thicknesses. A curve showing

the range of charge as a function of energy for 50% transmission was thus derived, and this curve was compared with existing theory and other empirical range-energy data.

I. INTRODUCTION

One aspect of the study of the interaction of radiation with matter has been the determination of range-energy relationships for charged particle beams. In the early experimental development of nuclear science, range data provided the principal means for measuring the energy of particle beams and nuclear decay products. The subsequent development of more accurate electrostatic and magnetic deflection techniques, scintillation spectrometers and solid state spectrometers rendered the direct application of range measurements to these purposes of less importance.

However, the differential rate of energy loss, $\frac{dE}{dx}$, as a function of energy and the related stopping cross-sections of the target material have assumed considerable importance as far as uses of tabulated data are concerned.[1] The precision with which nuclear reaction cross-sections can be determined depends a great deal on the accuracy with which the stopping cross-sections of target materials are known. A more recent application of energy-loss data is the study of nuclear reactions by the observation of recoiling nuclei. Frequently when a nuclear disintegration involves the emission of several particles, the only practicable method of recording events involves the measurement of nuclear recoil.[2] Another area of great interest currently is the study of radiation effects on

---

[1] W. Whaling, Handbuch der Physik, 34, 192 (1958).

[2] B. G. Harvey, Ann. Rev. Nucl. Sci. 10, 235 (1960).

solids, and investigators in this field acknowledge a need for additional data.[3,4]

In the intermediate and high-energy regions an extensive body of experimental data has been accumulated on range and stopping power in different media for heavy charged particles.[5] Theoretical development has kept pace with experiment and shows reasonable agreement over the entire range of energy from very low-energy particles in gaseous media to relativistic particles in solids.[6,7,8] However, in the energy region below 30 keV there is a marked lack of data for protons and alpha-particles, especially for solid absorbing materials. Table I presents a partial listing of relevant experimental work in this energy region.

Until very recently the lack of data has been equalled by a lack of theoretical treatment in this energy range. The Bohr and Bethe-Bloch formulations are known to be inapplicable. Several theorists have recently extended the theory of heavy charged particle interaction down into very low-energy regions using the Fermi-Teller gas model.

---

[3] F. Seitz and J. S. Koehler, Solid State Physics, Vol. 2, 305 (1955).

[4] D. S. Billington and J. H. Crawford, Radiation Damage in Solids, (Princeton University Press) (1961).

[5] R. E. Brown and N. Jarmie, LA-2156 Physics and Mathematics (TID-4500, 13th ed., Suppl.) (1958).

[6] A. E. Taylor, Rep. on Prog. in Phys. 15, 49 (1952)

[7] H. A. Bethe and J. Ashkin, Experimental Nuclear Physics, E. Segre, ed. (John Wiley and Sons, Inc., New York) Vol. 1, p. 166, (1953).

[8] S. K. Allison and S. D. Warshaw, Rev. Mod. Phys. 25, 779 (1953).

Table I

PREVIOUS EXPERIMENTAL WORK ON LOW ENERGY CHARGED PARTICLE ABSORPTION

Reference	Incident Particle and Energy Range	Absorber Material	Method	Results
Phillips, J.A.[a]	Protons $10 \leq E_p \leq 80$ keV	gases	Magnetically analyzed protons pass through gases confined in thin- window cells. Energy loss is measured by applying stopping potential to collector.	$\frac{\Delta E}{\Delta X} = L_i f(M_i E)$ for all gases if appropriate values of L_i, M_i are used.
Reynolds, et. al.[b]	Protons $30 \leq E_p \leq 600$ keV	gases	Electrostatically analyzed protons pass through thin window gas cell and energy loss is measured with magnetic spectrometer.	Stopping cross-sections determined.
Wilcox, H.A.[c]	Protons $60 \leq E_p \leq 400$ keV	Al, Au	Protons pass through self-supported films and energy loss is measured by electrostatic analyzer and electron multiplier tube.	Range-Energy curves and dE/dx.
A. Van Wijngaarden[d]	Protons $4 \leq E_p \leq 30$ keV	C, Al_2O_3 and VYNS	Magnetically analyzed ions penetrate self-supporting films. Energy loss is measured with electrostatic analyzer.	Found stopping cross-section $S_e = 4.3 \times 10^{-15} E^{0.45}$ eV cm^2 for Al_2O_3; also show few atomic collisions and few wide-angle deflections.

Table I (continued)

Reference	Incident Particle and Energy Range	Absorber Materials	Method	Results
Hines, R.L.[e]	Deuterons $5 \leq E_d \leq 27$ keV	Al, Cu and Au	Change in optical reflection coefficient of quartz due to radiation damage is measured and related to 50% penetration by incident particles through metal films evaporated onto quartz.	Tabular and graphed data are corrected for protons and plotted here. (See Fig. 17).
Young, J.R.[f]	Protons $1 \leq E \leq 25$ keV	Al	Thin aluminum films were supported on ZnS powder phosphor. Magnetically analyzed protons were incident on aluminum side and luminescence from the phosphor was a measure of transmitted energy.	$R(\mu)=0.02\ E(\mathrm{KeV})^{0.83}$ This function is plotted here (see Fig. 17).

(a) J. A. Phillips, Phys. Rev. 90, 532 (1953).

(b) H. K. Reynolds, et.al., Phys. Rev. 92, 742 (1953).

(c) H. A. Wilcox, Phys. Rev. 74, 1743 (1948).

(d) A. Van Wijngaarden and H. E. Duckworth, Can. J. Phys. 40, 1749 (1962).

(e) R. L. Hines, Phys. Rev. 132, 701 (1963).

(f) J. R. Young, J. Appl. Phys. 27, 1 (1956).

More extensive experimental work is required to substantiate these newer calculations which are discussed in the following section.

One of the primary reasons for this lack of data is the difficulty of constructing sufficiently thin self-supporting foils for range measurements. Work currently being carried on at ORNL on electron tunneling suggested the new approach employed here.

A metallic conductor (2) is evaporated onto a glass substrate to a thickness exceeding the possible range of protons of 30 keV energy. (See Fig. 1). An extremely thin layer of SiO is then evaporated onto the initial collector followed by (1) a layer of the metal to be studied. Light-weight current leads are soldered to each of the metallic layers. The beam is incident normally on the top metallic layer. The thin SiO layer provides sufficient electrical insulation between the two conducting layers so that charged particles stopping in one of the conducting layers will result in a current flow through a sensitive galvanometer connected between that layer and ground. The thickness of the top layer is measured interferometrically and the measured currents are analyzed to yield range information.

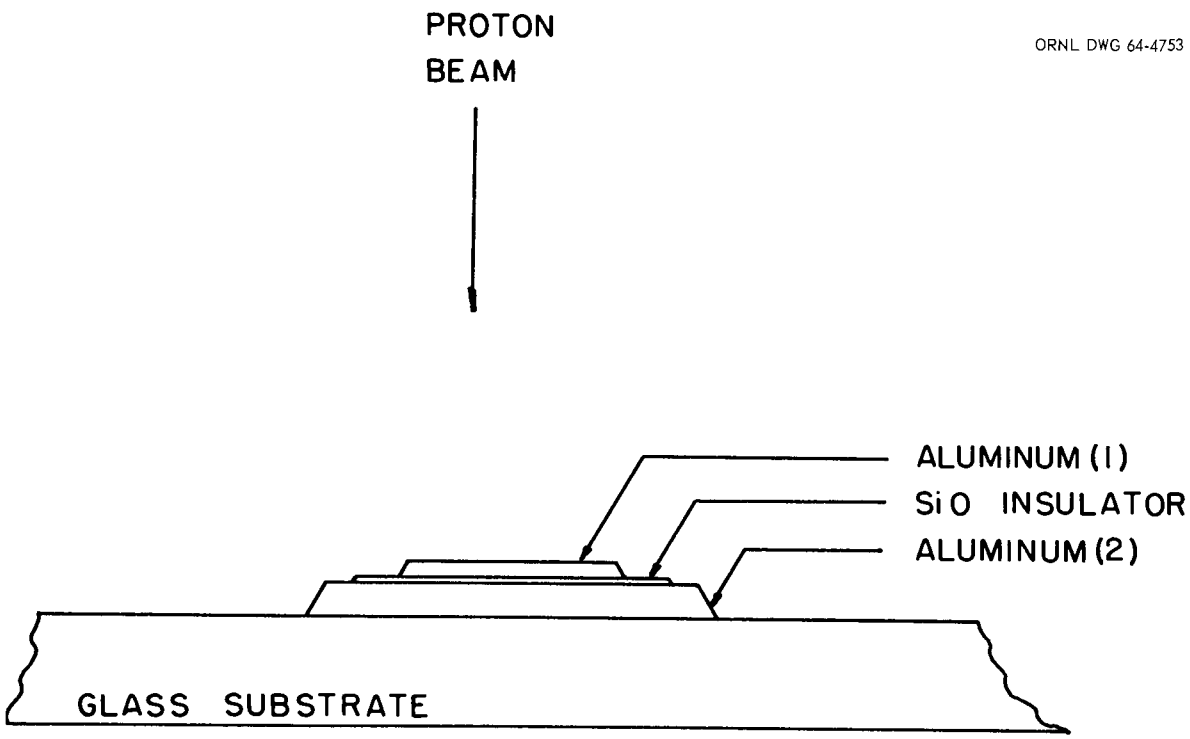

Fig. 1. Cross-sectional View of Evaporated Target (Not to Scale).

II. THEORY

A. Lindhard-Scharff Stopping Power Theory for Heavy Particles

In the kilovolt energy region, the slowing down of ions in matter is a complex phenomenon and is predicted theoretically only in an approximate manner. The incident ions may lose energy by ionization or excitation of electrons in the stopping material or by displacement of atoms of the material. In addition, the incident ions may lose energy in a few hard collisions and may be deflected through large angles. Thus the motion of the incident ions through the material is a diffusion phenomenon and this range straggling makes it necessary to broaden the concept of range to include a mean penetration depth.[9]

For ions with velocity $v \leq v_o = e^2/\hbar$, (v_o = the velocity of the electron in the first Bohr orbit of hydrogen) or for protons at energy $E \leq 25$ keV, competition for energy loss occurs between electronic collision and atomic recoil. The corresponding stopping cross-sections, S_e and S_n, are related to the differential energy loss $\frac{dE}{dx}$ by the equation

$$\frac{dE}{dx} = - NS \tag{1}$$

where N is the number of stopping atoms per unit volume in the absorber, and the total stopping cross-section is $S = S_e + S_n$.

---

[9] R. L. Hines, Phys. Rev. 132, 701 (1963).

The energy dependence of S_e has been calculated using the Fermi-Teller model[10] which assumes that the incident ion moves through an electron gas of uniform density. J. Lindhard and M. Scharff[11,12] have found that the electronic stopping cross-section is proportional to velocity at low velocities, i.e., where $v \leq Z_1^{2/3} v_o$, and have derived the variation with Z_1 and Z_2, the atomic numbers of the incident ion and of the stopping material respectively. To a first approximation they found

$$S_e = \xi_e \, (8\pi \, e^2 a_o) \left[\frac{Z_1 Z_2}{(Z_1^{2/3} + Z_2^{2/3})^{3/2}} \right] \left(\frac{v}{v_o}\right) \qquad (2)$$

where ξ_e is the ratio of the screening parameter a, to the collision approach parameter b, and has a value of the order 1-2; a_o is the Bohr radius of the hydrogen atom which is equal to $\frac{\hbar^2}{me^2} = 0.529 \times 10^{-8}$ cm. For $v \geq v_o \, Z_1^{2/3}$ formula (2) is no longer valid, and the stopping cross-section will reach a maximum and decrease at higher velocities and S_e vary approximately as $\frac{\ln E}{E}$ according to Bloch's[13] quantum mechanical treatment for intermediate energies.

Powers and Whaling[14] have suggested the value $Z_1^{1/6}$ for ξ_e and, if this is accepted, equation (2) can be written

---

[10] E. Fermi and E. Teller, Phys. Rev. 72, 399 (1947).

[11] J. Lindhard, Kgl. Danske Videnskab Mat. Fys. Medd. 28, No. 8, (1954).

[12] J. Lindhard and M. Scharff, Phys. Rev. 124, 128 (1961).

[13] F. Bloch, Ann. Physik, 16, 285 (1933).

[14] D. Powers and W. Whaling, Phys. Rev. 126, 61 (1962).

$$S_e = Z_1^{1/6} (8\pi e^2 a_o) \left[\frac{Z_1 Z_2}{(Z_1^{2/3} + Z_2^{2/3})^{3/2}}\right] \left(\frac{E}{E_o}\right)^{1/2} \qquad (3)$$

where E_o is the kinetic energy of the incident heavy particle when it has velocity v_o, or 25 keV for protons.

The stopping cross-section for atomic collision S_n can be derived following the outline presented by Van Wijngaarden and Duckworth.[15] Niels Bohr first studied the form of S_n and assumed it was nearly constant in a considerable velocity interval at low velocities.[16] Bohr suggested that incident particles will collide elastically with atoms in a potential

$$V(r) = \frac{e^2 Z_1 Z_2 e^{-r/a}}{r} \qquad (4)$$

where r is the distance between the incident ion and the target atom and a is the electronic screening parameter. Lindhard and Scharff[17] considered a Rutherford scattering model and used a value for the screening parameter

$$a = \frac{0.8853\, a_o}{(Z_1^{2/3} + Z_2^{2/3})^{1/2}} \qquad (5)$$

The distance of closest approach b' in a head-on collision in this type of potential is given by

$$\frac{b}{a} = \frac{b'}{a} e^{b'/a} \qquad (6)$$

---

[15] A. Van Wijngaarden and H. Duckworth, Can. J. Physics, 40, 1749 (1961).

[16] N. Bohr, Kgl. Danske Videnskab. Selskab Mat. Fys. Medd. 18, No. 8, (1948).

[17] J. Lindhard and M. Scharff, loc. cit.

where b is the distance of closest approach if the colliding atoms were stripped of their electrons and has the value

$$b = 2Z_1Z_2e^2 \left\{ \frac{M_1 + M_2}{M_1M_2 \; v^2} \right\} , \tag{7}$$

M_1 and M_2 being the masses of the incident ion and target atoms respectively.

In the case where a Coulomb potential is a good approximation and the scattering is predominantly of the Rutherford type, then $\frac{b'}{a} \ll 1$ and $b' \rightarrow b$. In this energy region Bohr found S_n to be given by

$$S_n = 2\pi \frac{M_1}{M_2} e^4 \frac{Z_1^2 Z_2^2}{E} \ln \left\{ \frac{2a}{Z_1Z_2e^2} \frac{M_2}{M_1 + M_2} E \right\} \tag{8}$$

As energy decreases, $\frac{b'}{a}$ increases in value and scattering occurs more frequently in the screened part of the field. When $\frac{b'}{a} \sim 1$, the scattering potential is approximately inverse square rather than Coulombic. In the energy range of this experiment $\frac{b'}{a}$ is less than 0.5 and equation (8) is a valid expression for computing S_n.

For completeness it should be noted that Lindhard and Scharff[18] give an expression for S_n when $E \leq E_o$ and $\frac{b}{a} \gtrsim 1$ although the latter restriction is not satisfied in the case of the present experiment.

$$s_n = \xi_n \frac{\pi^2}{2} e^2 a \, Z_1Z_2 \left\{ \frac{M_1}{M_1 + M_2} \right\}$$

where

$$\xi_n = \frac{2}{2.718 \times 0.885}$$

$$a = \frac{\hbar^2}{me^2} \times 0.885 \, (Z_1^{2/3} + Z_2^{2/3})^{-1/2} \tag{9}$$

---

[18] J. Lindhard and M. Scharff, loc. cit.

An evaluation of Eqn. 8 yields the result:

$$S_n = \frac{81.5 \times 10^{-22}}{E(eV)} \ln\left[1.87 \times 10^{-3}\, E(eV)\right] \tag{10}$$

in units of eV cm^{-3} $\mathring{A}^{-1}$. The notation E(eV) indicates that the energy is to be entered into the equation in electron volts. The electronic stopping cross section can be evaluated from equation (3) and yields the value:

$$S_e = 94.1 \times 10^{-26} \sqrt{E(eV)} \tag{11}$$

The nuclear recoil stopping cross-section is small in the energy range of this experiment, and an expression for the absolute range of protons in aluminum can be computed from

$$\frac{dE}{dx} = - NS_e. \tag{12}$$

N for aluminum is 0.602×10^{23} atoms/cm^3 and formula (12) is thus:

$$-\frac{dE}{dx} = 5.66 \times 10^{-2} \sqrt{E(eV)} \tag{13}$$

in units of eV $\mathring{A}^{-1}$. Integrating dE from E_o to 0 and dx from 0 to R yields, the range in $\mathring{A}$;

$$R(\mathring{A}) = 35.3 \sqrt{E(eV)}\ . \tag{14}$$

Values are calculated from this formula and plotted in Figure 17 for comparison with our data and other experimental range-energy curves.

B. Analysis of Current Energy Curves and Definition of Range of Charge

The target foils and associated galvanometer system employed here are sensitive to the incident particles only while they are charged. If a proton passes from the front layer to the back, it may do so as a charge + 1 or as a neutral. In the latter case the front layer has lost one electron and thus appears to have gained a proton, while

the back layer receives no net charge. It is convenient to analyze this current data using the following formulation:

$T(E)$ = transmission fraction for protons of incident energy E

$f_o(E)$ = fraction of protons of incident energy E emerging from front layer with zero charge

$f_+(E)$ = fraction of protons of incident energy E emerging from front layer with + 1 charge

The sum of the top and bottom currents must equal the sum of the incident proton and molecular hydrogen ion currents,

$$i_T + i_B = i_P + i_{H_2} \tag{16}$$

Upon incidence into the foil, the hydrogen molecular ion component dissociates into a proton and a neutral hydrogen atom, each sharing the initial energy equally.

$$H_2^+ \rightarrow P^+ + H_1^o \tag{17}$$

The top and bottom currents can be expressed as sums of terms utilizing the above definitions and the fact that $f_o + f_+ = 1$.

$$\begin{aligned} i_T(E) &= \left[1 - T(E)\right] i_P + \left[T(E)\ f_o\ (E)\right] i_P + \left[1 - T(E/2)\right] i_{H_2} \\ &+ \left[T(E)\ f_o(E/2)\right] i_{H_2} - \left[T(E/2)\ f_+\ (E/2)\right] i_{H_2} \\ i_B(E) &= \left[T(E)\ f_+(E)\right] i_P + \left[2T(E/2)\ f_+(E/2)\right] i_{H_2} \end{aligned} \tag{18}$$

It is interesting to note that in the case of high energy, $T(E) \rightarrow 1$, $f_o = 0$, and $f_+ = 1$. The current to the top layer that is measured is simply the negative term above.

$$\lim_{E \rightarrow \infty} i_T(E) = - i_{H_2} \tag{19}$$

Thus the total hydrogen molecular ion component in the beam can be read from the constant negative portion of the normalized plot of current to the top collector. (Fig. 14, a, b, c.).

We define $T(nE)f_+(nE)$ as the range-of-charge parameter and calculate a curve of this quantity against energy. We write the expression for current to the bottom collector as follows:

$$i_B(2nE) = \left[T(2nE)f_+(2nE)\right] i_P + \left[2T(nE)f_+(nE)\right] i_{H_2} \qquad (20)$$

We choose a low value, say 0.5 keV, for 2nE from Figure 14 and assume $T(nE)f_+(nE) \rightarrow 0$, at half that energy. Then

$$T(2nE)f_+(2nE) \cong \frac{i_B(2nE)}{i_P} \qquad (21)$$

For twice the value of energy chosen initially for 2nE, the second term in Eqn. 20 is given by Eqn. 21 and the first term can again be calculated. This now may be used in the second term when the energy is again doubled and so on. Thus a set of values for proton transmission as a function of energy can be calculated. Figures 14 a, b, and c are analyzed in this manner and calculated values are plotted for each foil in Figure 15. A value of energy is chosen from Figure 15 at which 50% of the incident protons are transmitted for each of the three aluminum thicknesses, and a plot of this energy versus the thickness for $T(E)\ f_+(E) = 0.5$ is presented in Figure 16.

III. EXPERIMENTAL APPARATUS AND PROCEDURE

A. Radio-Frequency Ion Source

The proton beam is extracted from a radio-frequency ion source similar to that described by Allison and Norbeck.[19] (See Figures 2 and 3). Hydrogen gas is fed into the pyrex glass discharge vessel from a variac-controlled paladium diffusion tip inserted into a tank containing gas at about two atm. pressure. (See Figure 4.) A plasma is excited in the vessel by the r.f. coil. The oscillator used here generates a rms voltage of 870 v., operates at a frequency of 49.8 Mc/sec, and is capable of establishing a continuous plasma over a wide range of pressures (2μ - 1000μ) without initial excitation.

Positive ions are accelerated toward the beam port by a positive potential applied to a 0.020" o.d. tungsten wire anode embedded in the top of the discharge vessel. The anode is fitted with a vaned aluminum cylinder outside the vacuum for heat dissipation. A pyrex glass electron shield is mounted just below the expulsion anode to to prevent excessive heating of the discharge vessel. The aluminum cathode and beam port is removable to allow for changing the hole size which permits varying the pressure differential between the discharge tube and the target area. A Hastings thermocouple vacuum gauge type DV-3M is positioned in the copper hydrogen gas line near the vessel gas inlet.

---

[19] S. K. Allison and E. Norbeck, Rev. Sci. Inst. 27, 285 (1956).

ORNL PHOTO 64804

Fig. 2. Photograph of Experimental Apparatus.

ORNL DWG 64-4386

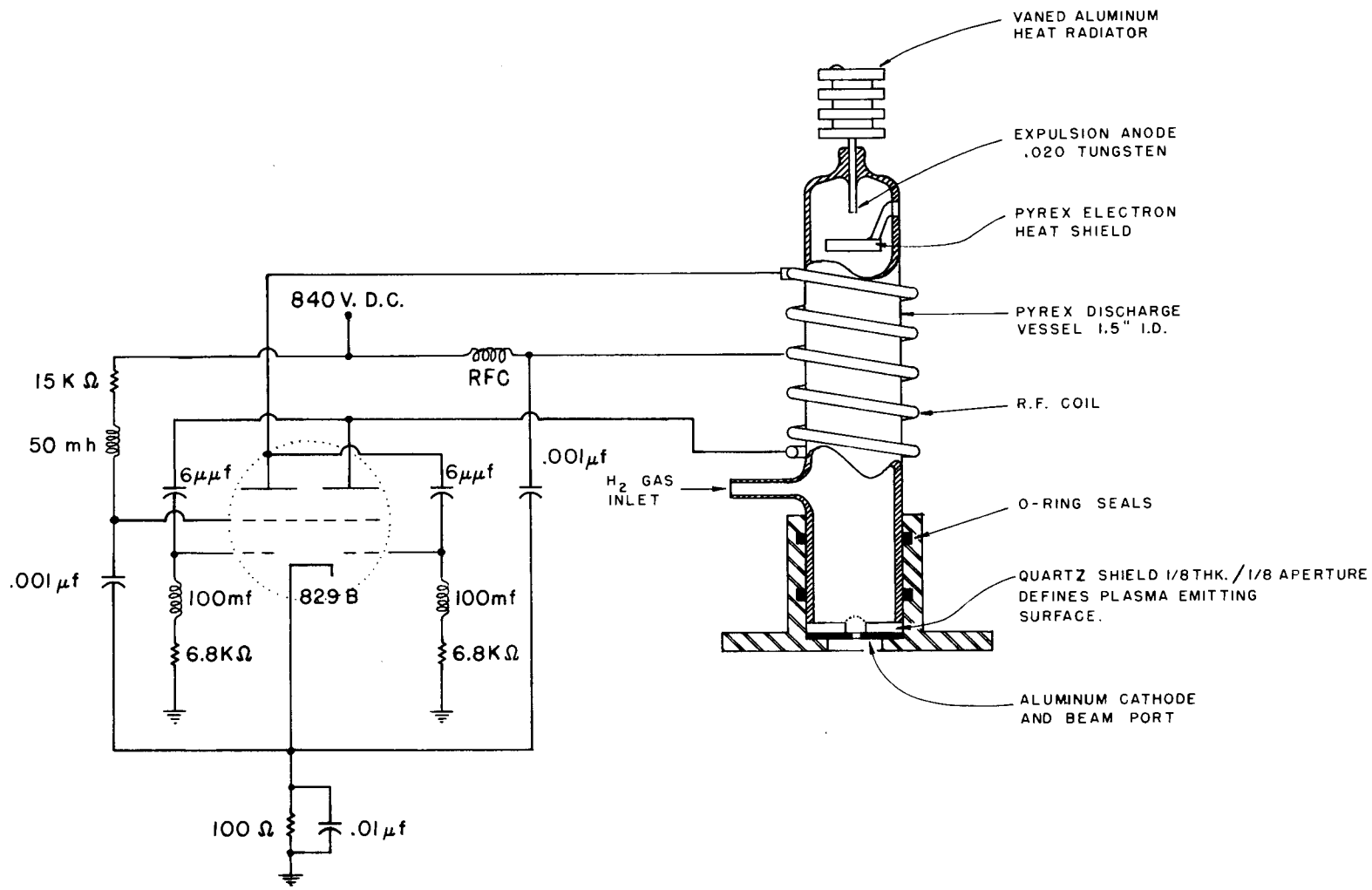

Fig. 3. Diagram of R-F Ion Source and Oscillator Circuit.

ORNL DWG 64-4433

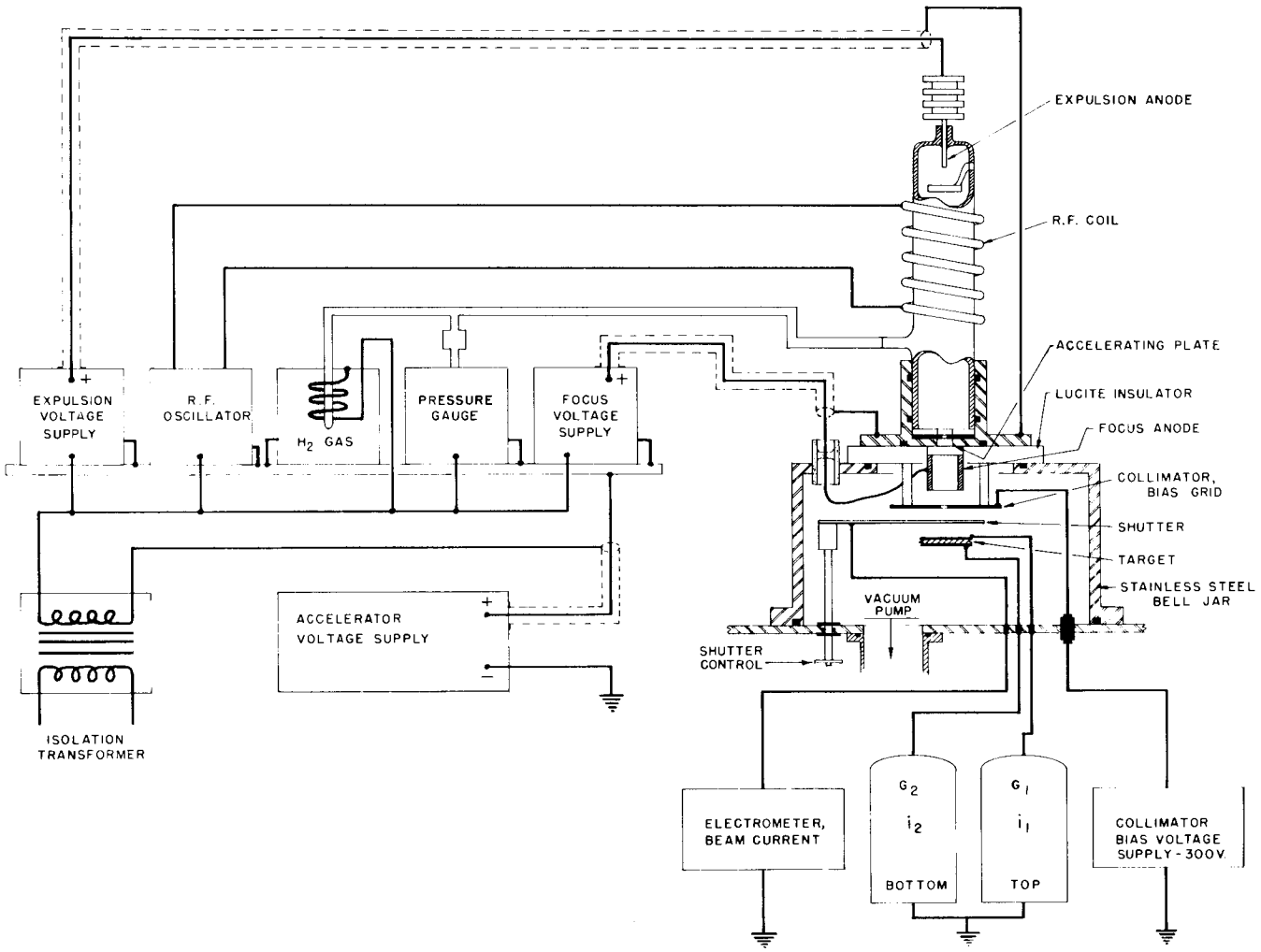

Fig. 4. Schematic Diagram of Experimental Apparatus.

A quartz disk shield is aligned coaxially and in contact with the cathode exit port and has a dual function. Recombination occurs in the plasma resulting in a molecular hydrogen ion (H_2^+) component in the extracted beam. Metal surfaces are better catalysts than quartz for recombination; the recombination coefficient for metals is about 1, compared to 7×10^{-14} for quartz.[20] Thus the quartz shield reduces the metal surface exposed to the plasma and increases the proton purity of the beam. Secondly, the quartz disk becomes electrostatically charged, and near the central aperture, field lines extending into the plasma produce a spherical equipotential surface. Positive ions are emitted from the plasma normal to this surface and the field assists in channeling the ions through the exit port.

A positive ion current (equal to 1.5 μa) is generated by the source by an extraction potential to 2 kV for a H_2 gas pressure of 20μ.

B. Accelerator, Expulsion and Focus Anode Circuit, and Procedure for Beam Energy Analysis

Ions emerging from the exit port have attained an energy slightly less than the product of their charge and the potential difference between the expulsion anode and the accelerating plate and exhibit a small spread of energy values below the maximum due to diffusion through the plasma. The expulsion voltage which results in the smallest energy spread is 2000 V. (See Figure 6.) The beam passes through a cylindrical focusing anode which functions as an electrostatic lens.

---

[20] C. D. Moak, Nucleonics 9, No. 3,18 (1951).

The field lines focus the beam axially, and control of beam current on the collimator aperture is possible by varying the potential on the focus anode.

The expulsion and focus anode potentials are supplied by a dual output high voltage supply capable of 5000 V. on each output. (See Figure 4.) A Sorensen High Voltage Supply, model 1061, provides additional potential for accelerating ions up to 30 keV. This voltage is fed into the negative side of the dual expulsion and focus anode supply, and the shielded high voltage leads to these anodes are connected to the aluminum accelerating plate. The dual voltage supply as well as the r.f oscillator supply, the thermocouple gauge meter, and the hydrogen gas supply are floated above ground at the voltage applied by the Sorensen. These instruments are insulated from ground through an isolation transformer which provides the 110 V. line voltage at high DC voltage. Thus for a beam energy of 20 keV, the Sorensen voltage is 18 kV, the expulsion anode is at 20 kV, and the focus anode will be some value between 18 and 20 kV. An ion in the plasma accelerates through a voltage drop from the 20 kV at the expulsion anode to 18 kV on the accelerating plate, and then receives an additional 18 keV between the accelerating plate and the target foil at ground.

The distribution of energy in the proton beam was determined by applying a stopping potential to an aluminum collector plate located in the same position occupied by the target foils during current measurements. (See Figure 5.)

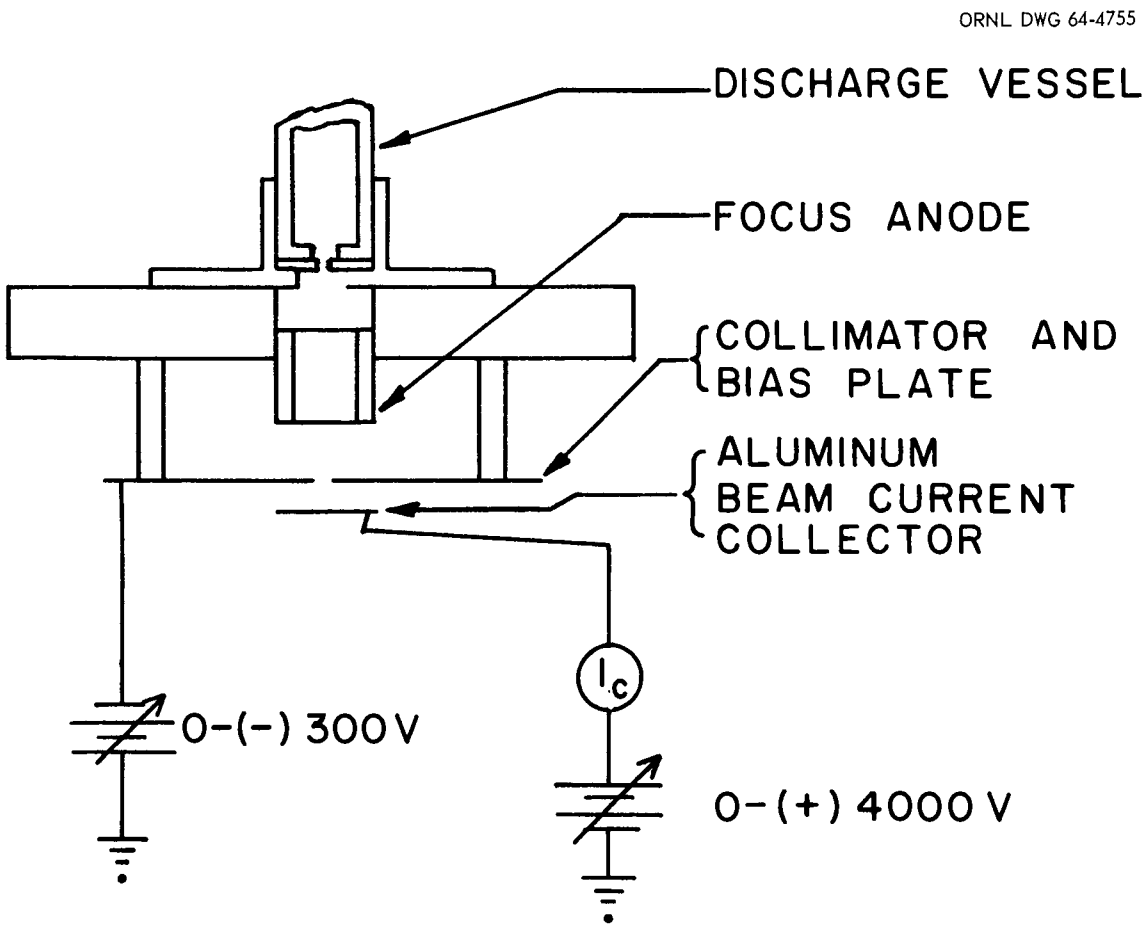

Fig. 5. Schematic Diagram of Apparatus for Measurement of Energy Distribution in Beam.

Beam energy was established at 4 keV by applying 2 kV to the expulsion anode and an additional 2 kV accelerating potential to the base. The focal control was adjusted for a beam current of .15 μa used typically in foil bombardment. A retarding potential was applied to the collector, and current to the galvanometer was read as this voltage was increased. A graph of collector current vs stopping potential indicates a 200-eV energy spread with a maximum at 3.9 keV. (see Figure 6.)

The initial sharp drop in current was caused by secondary electrons ejected from the collector by incident ions. Negative suppressor voltage was applied in small steps to the collimator to determine the saturation point for secondary emission. Collector current is plotted against secondary electron suppressor voltage in Figure 7. During current measurement on the evaporated targets a collimator voltage of -200 V was applied. At energies of 30 keV a voltage of at least -125 V required to completely suppress secondary emission from the aluminum foils.

C. Collimator and Secondary Electron Bias Plate

The collimator and bias plate is a 5" diameter stainless steel disk, 0.025" thick with a 3 mm. diameter aperture centered coaxially with the exit port and focus anode. (See Figure 4.) It is mounted to the lucite ion source base by lucite insulating standoffs. A secondary electron negative bias voltage is supplied to the collimator by an Oregon high voltage supply. The collimator is positioned about 1 cm above the target foil. No net energy change is experienced by ions passing through the collimator.

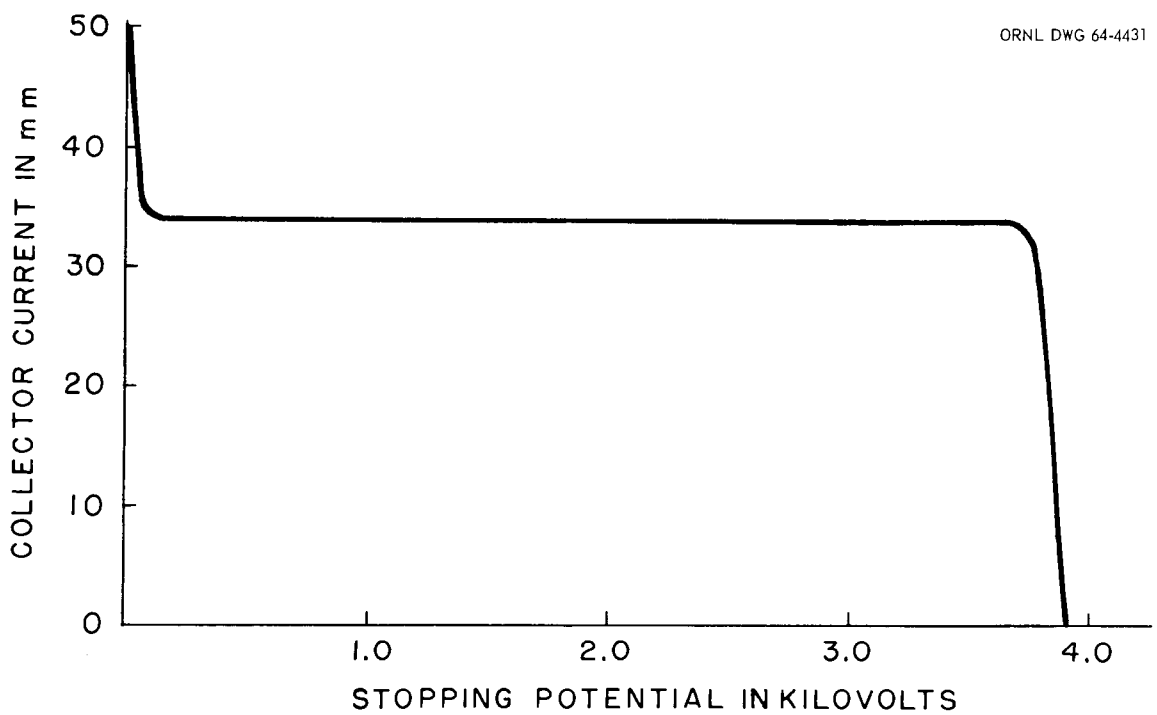

Fig. 6. Collector Current versus Stopping Potential for Measurement of Beam Energy Distribution.

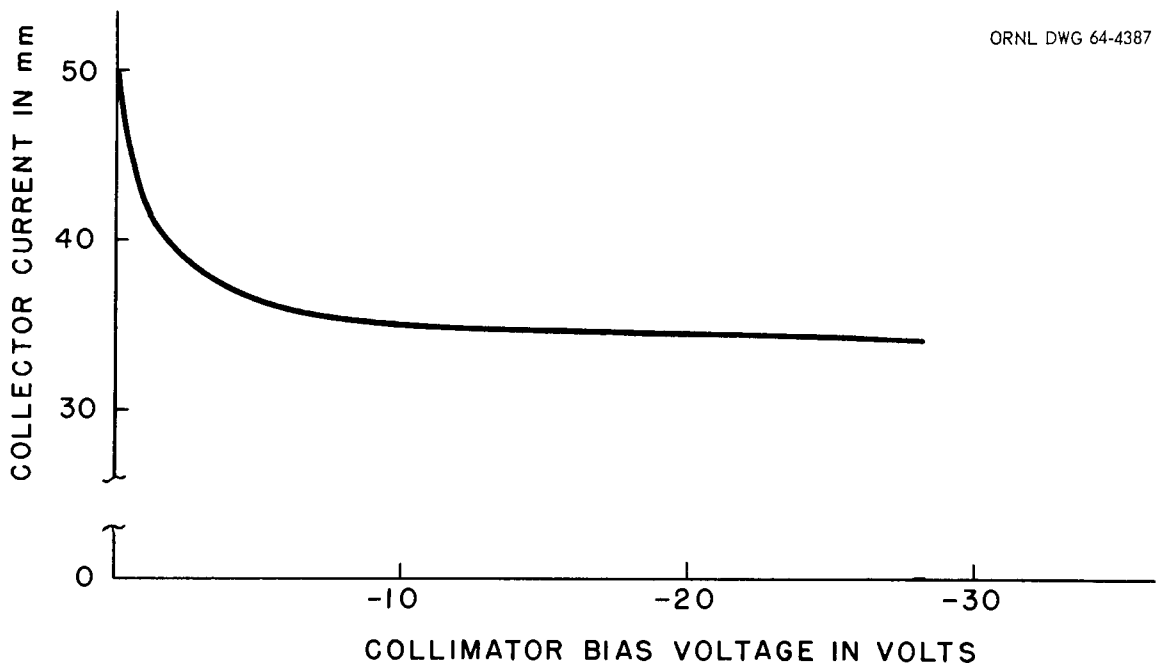

Fig. 7. Collector Current versus Collimator Voltage for Suppression of Secondary Electron Emission from Collector.

D. Target Foil Design and Evaporating Apparatus

Foils are evaporated onto a standard 4" x 3" glass cover slide carefully cleaned and heat dried prior to evaporation. (See Figure 8.) The evaporation apparatus is provided with a cathode ring centered on the glass substrate. A gas discharge is established at 2 kV at a pressure of 35μ to effect additional cleaning and surface outgassing of the substrate by ionic bombardment. A series of masks and templates are mounted close to the substrate and are positioned via control rods external to the vacuum system.

The initial step is a silver-manganese alloy evaporation which provides electrical contacts for the top and bottom aluminum layers. Light-weight current leads are soldered to the silver-manganese contacts using a low temperature indium solder. The bottom layer of aluminum (2) is evaporated to an "infinite" thickness (> 2000 Å) for 30-keV protons, from a cylindrical tantalum source (see Figure 9). Since there is higher resistance to current flow near the aperture in this evaporating source, there is greater heating near the center. Molten aluminum is observed to flow towards the cooler areas of a source, and thus is contained near the crimped ends of the tantalum tube. Several deflections of the vapor particles which eventually condense on the substrate are therefore required, and this insures an atomic vapor, which reduces excessive graininess of the surface and stops sputtered agglomerates from reaching the substrate. Uniform and smooth surfaces are necessary in order to prevent low resistance current paths through the very thin silicon monoxide layer. The silicon monoxide layer is evaporated from a boron-nitride crucible heated by a tantalum wire

ORNL PHOTO 65087

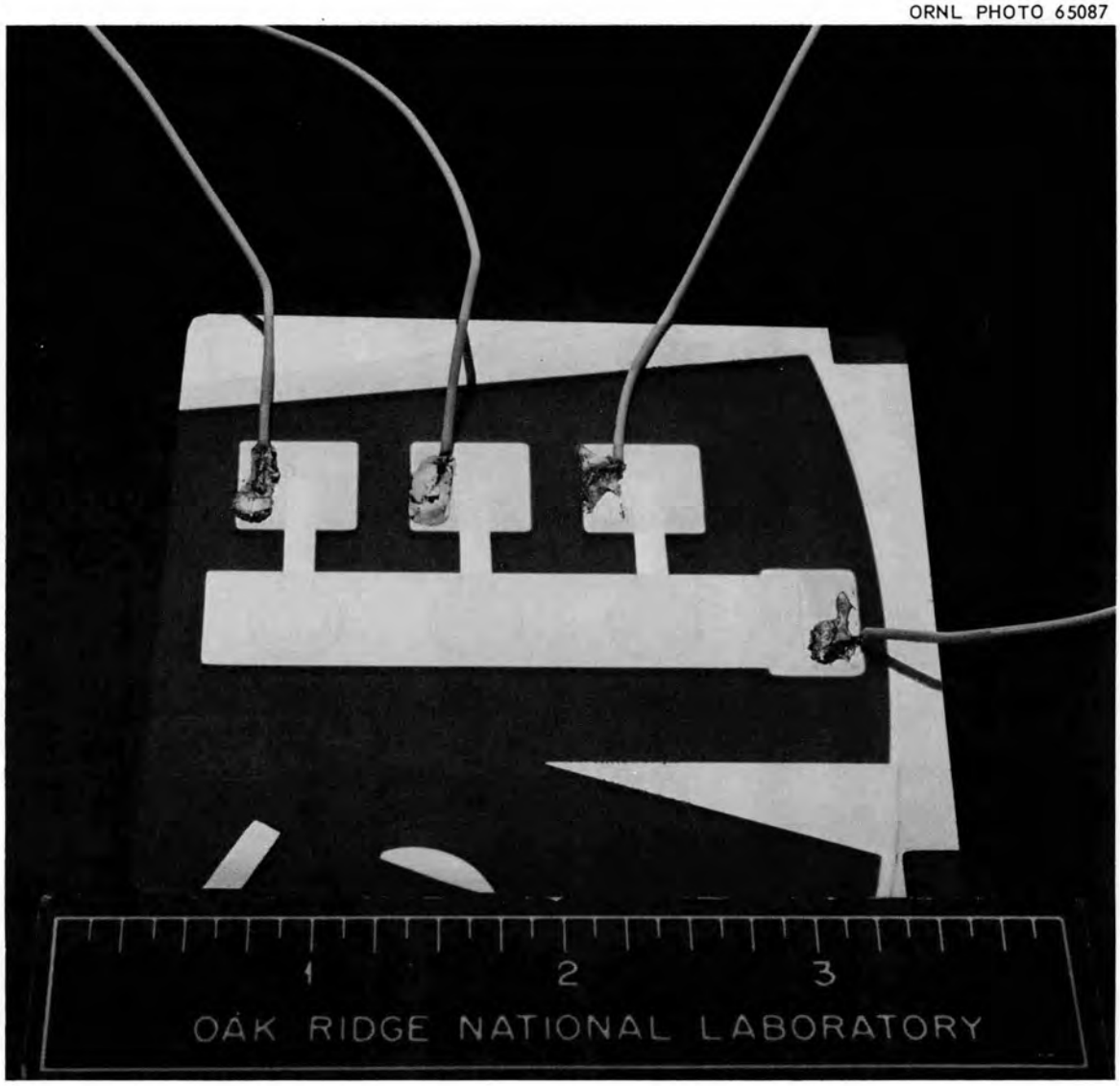

Fig. 8. Photograph of Evaporated Target.

ORNL DWG 64-4752

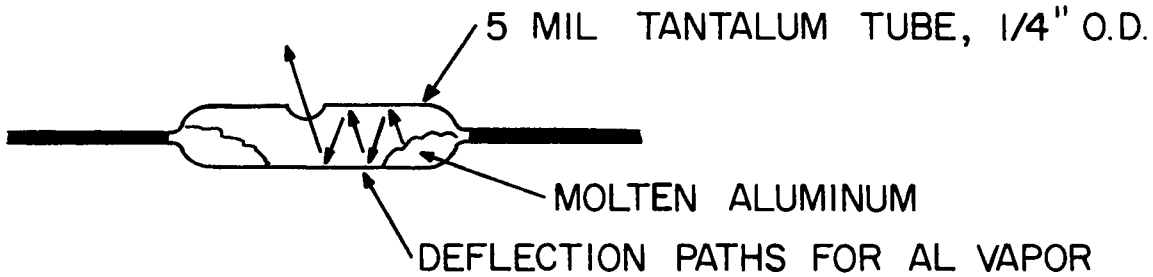

Fig. 9. Diagram of Evaporating Source for Aluminum.

wound coil and provided with a heated tantalum tube deflection chamber. (See Figure 10.)

The top aluminum layer is evaporated from the tantalum source shown in Figure 9.

The evaporating apparatus is contained in an 18" diameter by 24" high glass bell jar evacuated by a 4" oil diffusion pump backed by a Welch forepump. The vacuum system utilizes a liquid nitrogen cold trap to condense residual vapors and a cooled chevron baffle to prevent back-streaming of oil vapor. The bell jar and electrodes are carefully cleaned prior to each target fabrication to prevent contamination of evaporated layers. All evaporations are conducted at pressures below 5×10^{-5} mm Hg. Sources are positioned about 20 cm from the substrate to insure uniform thickness of the layers and prevent excessive radiative heating of the substrate. All sources are preheated (with the substrate shielded) to outgas impurities.

E. Current and Resistance Measuring Circuits and Procedure for Resistance Regeneration

Beam particles stopping in the top or bottom aluminum layers are detected by measuring the positive current from each with two Leeds and Northrup D-C galvanometers, Model 2430. (See Figures 4 and 11.) The galvanometers are shunted with 440 Ω damping resistors and present 22 Ω paths to ground from each aluminum collector. The instruments were calibrated frequently using a known current source and had the following sensitivities: G_1, 0.00437 μa/mm; G_2, 0.00313 μa/mm. Each galvanometer casing is guard grounded.

The electrical resistance between the two aluminum layers is

ORNL DWG 64-4756

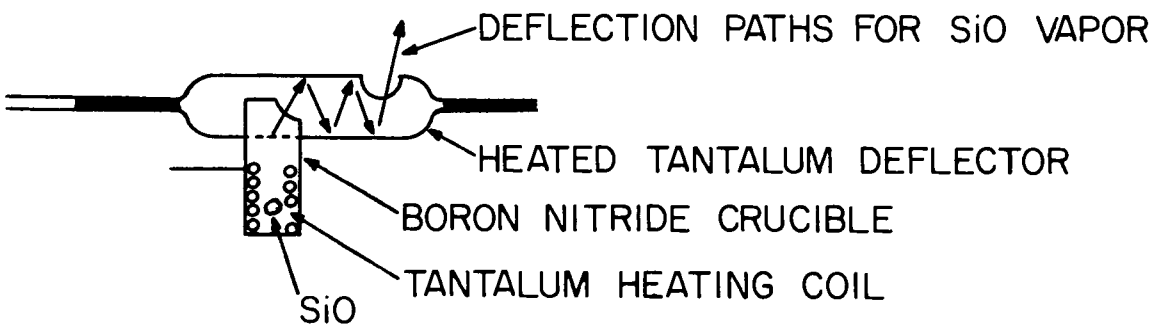

Fig. 10. Diagram of Evaporating Source for Silicon Monoxide.

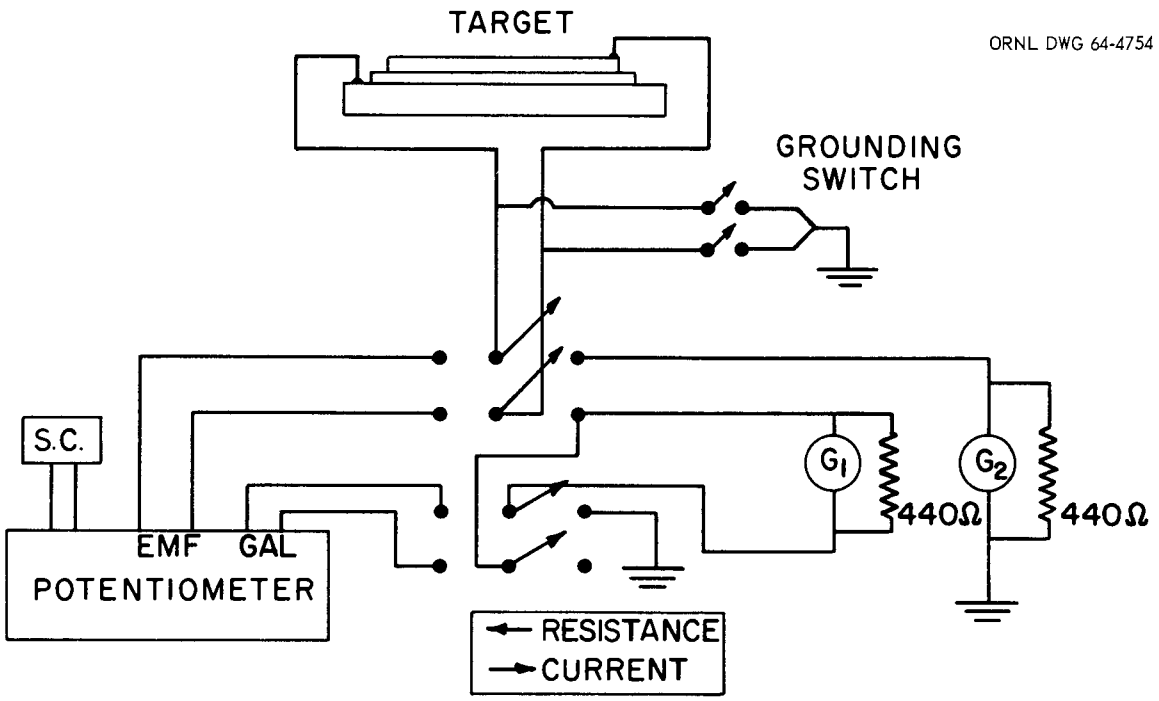

Fig. 11. Target Current and Resistance Measuring Circuit.

measured frequently during data runs to insure that radiation damage in the SiO layer has not occurred. A Leeds and Northrup potentiometer, Model 7553, type K-3, is used in conjunction with galvanometer 1. (See Figure 11.) A potential is applied across the silicon monoxide by the potentiometer and the resulting current passing between the aluminum layers yields the foil resistance if it is large compared to the internal resistance of the potentiometer (~ 180 ohm). The potentiometer supplies from 0 to 1.5 volts and is standardized with a 1.01871-V standard cell.

A switching circuit is provided which allows rapid resistance measurement and grounds both aluminum collectors during the change from beam current to resistance measuring positions. (See Figure 11.) Typical foil resistances are in the megohm region, though lower resistances can be used.

A shutter is provided which is positioned by an external control rod utilizing a rotating O-ring vacuum seal (see Figure 4). Total beam current was measured prior to target exposure using a Keithley electrometer, Model 414, and it agreed well with the sum of currents measured in the top and bottom layers.

Currents to the target collectors are measured when the shutter is rotated out of the beam path. Current is regulated prior to exposure to a maximum of 0.15 μa, and exposure times are limited to several seconds to avoid radiation damage to the SiO insulating layer. Figures 14, a, b, and c are normalized curves of top and bottom currents as a function of energy for several targets. Target resistance is monitored frequently during current runs.

Occasionally target foils have insufficient resistance between the aluminum layers due to conducting bridges across the SiO layer. In several cases these shorts were successfully removed by passing large currents from a charged 40 μF capacitor between the aluminum layers in a short time. The very narrow conducting paths were presumably burned out,[21] restoring sufficient resistance between the aluminum layers without causing further damage to the SiO.

F. Optical Interferometer for Thickness Measurement

The thicknesses of the top aluminum layers were measured using an interferometric method. This method utilizes the interference pattern produced when a light beam is reflected from two adjacent metal surfaces which are displaced from each other by a height equal to the thickness of the film being measured. The displacement of the break in the fringe pattern is then simply related to the height of the step in the surface.

The measurement is made on a section of film evaporated onto the substrate very near the target region. A sharp step is formed during evaporation by masking a portion of the substrate with a thin tantalum foil. An opaque coating of silver is evaporated over the surface of the metal and adjacent substrate. Since an evaporated layer accurately contours the surface of the substrate, this procedure provides a sharp step displacement in the silver coating equal to the film thickness. This surface is then matched against another surface on which a slightly

---

[21] D. Meyerhofer and S. A. Ochs, J. App. Phys. 34, 2535 (1963).

transmitting silver layer has been evaporated. The combination is then illuminated with monochromatic light, and the back-reflected fringe pattern is observed.

A diagram of the apparatus is shown in Figure 12. The light source was a mercury arc lamp producing an intense line spectrum. The 5461-Å and the 4358-Å lines were used and were isolated from the spectrum by means of interference filters. The fringe shift was observed with a Leitz Panphot photomicrograph and recorded with a Polaroid camera. It was necessary to focus by tilting the slides containing the step because the ring condenser delivers the light to the microscope stage at a slight angle.

Since the fringes are one-half wavelength apart, the thickness of the step is given by:

$$d = f \frac{\lambda}{2} \tag{22}$$

where f is the fractional displacement of the fringe shift. In the case of foils whose thicknesses are near some multiple of a quarter wavelength, there could be an uncertainty in the thickness determination because of the uncertainty in the direction of movement of the fringe shift. This difficulty is resolved by observing the same fringe pattern using a different spectral line. One of the two possible thicknesses determined will be common to both sets and this is the correct value. Typical fringe shift patterns for a 475-Å aluminum foil photographed using the blue and green mercury lines are shown in Figure 13.

The precision with which a step can be measured is dependent upon how well the fringe pattern can be focused. The width of a

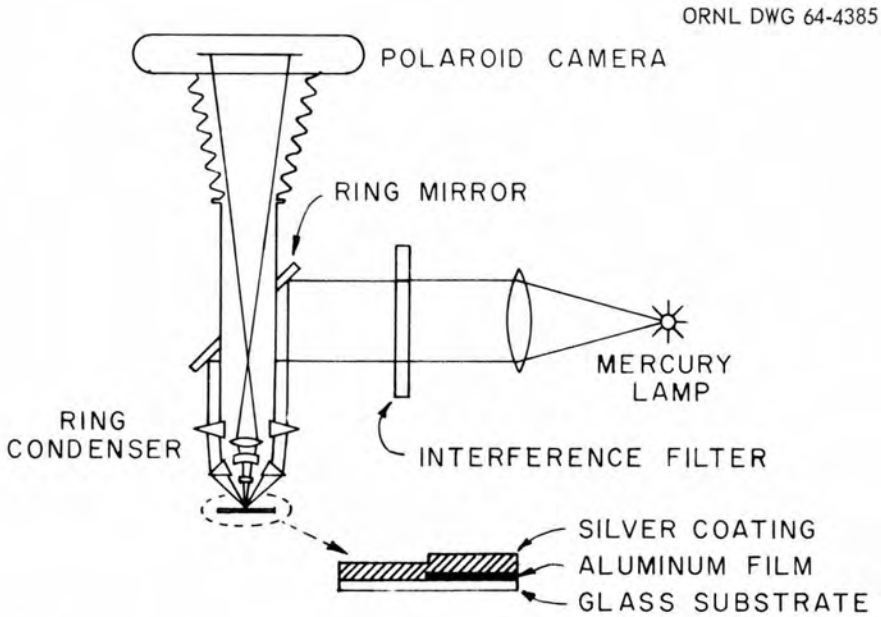

Fig. 12. Schematic Diagram of Optical Interferometer.

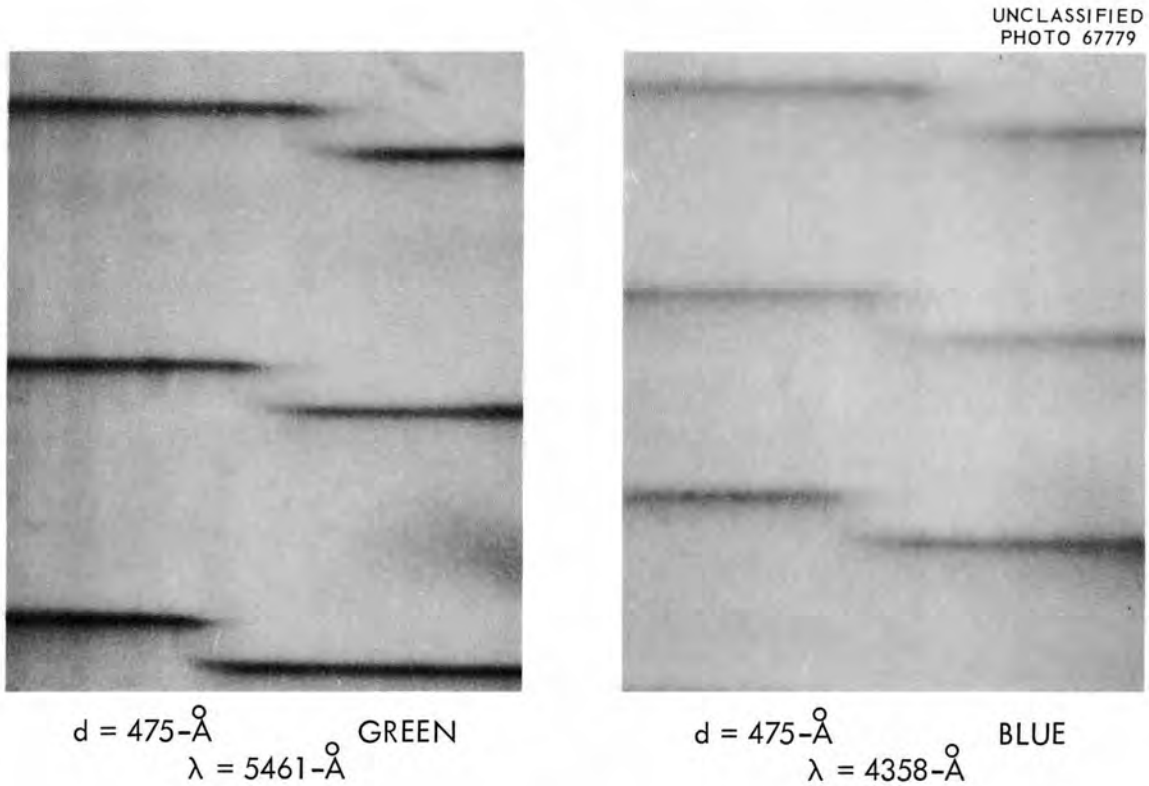

Fig. 13. Photograph of Fringe Shift for an Aluminum Foil, 475 Å Thick.

well-focused fringe is about 3% of a spacing. This represents about 80 Å in a typical case. Since it is a simple matter to locate the center line of a fringe to within 10 or 20%, it is possible to determine the thickness of a step to within 10 or 20 Å.[22]

G. Thin Film Thickness Monitor

An Edwards High Vacuum Ltd. thin film thickness monitor, model FTM I, is used during evaporation of the silicon monoxide and top aluminum layers. The monitor was calibrated on all scales for aluminum using the interferometric methods previously described, and on the 500-Å range scale for SiO.

The principle of operation is as follows: when a film is evaporated onto the flat surface of a vibrating quartz crystal, the crystal's effective mass is increased and its frequency of oscillation will decrease. The frequency change is linearly related to the mass deposited, and since the area of crystal exposed is constant, to the thickness of the film. The frequency shift is converted using two reference frequencies, one an identical vibrating crystal and the other a variable inductance and capacitance controlled circuit. The frequency shift is presented to a pulse analog type counter circuit, the output of which is shown on a moving coil meter.

The vibrating crystal housing is positioned as near as possible to the target area to be evaporated, and the geometry of placement is reproducible. Comparison of the monitored aluminum thickness and the interferometrically measured thickness showed agreement to within 10% on all foils.

---

[22] L. C. Emerson, E. T. Arakawa, R. H. Ritchie and R. D. Birkhoff, ORNL 3450 (1963), (unpublished).

H. Silicon Monoxide Thickness Determination by Neutron Activation

An optimal thickness for the SiO layer providing sufficient resistance and negligible absorption appeared to be approximately 75 Å. Since interferometric and weighing methods are inaccurate at this extreme, a neutron activation-beta counting method was investigated.

SiO samples are weighed using an electro-micro-balance and then irradiated to saturation in the ORNL Low Intensity Test Reactor. The reactions of interest are:

$$_{14}Si^{30} + n \rightarrow {}_{14}Si^{31} + \gamma$$

followed by

$$_{14}Si^{31} \rightarrow {}_{15}P^{31} + \beta^- \qquad (23)$$

$$\sigma = 0.11 \times 10^{-24}\ cm^2$$

$$T_{1/2} = 2.6\ hr$$

$$E_\beta = 1.486\ MeV$$

These bulk samples are then counted for beta activity in a G. M. counting system using a calibrated aluminum absorber, 1643 mg/cm^2, to reduce the count rate and coincidence loss. After evaporation of the initial sample, the targets are scanned for activity; and after geometry, time decay, and coincidence corrections, the ratio of count rates indicates the fraction of initial mass which has been deposited on the substrate. The area of the insulating layer is easily measured, and, since the distance of the substrate from the evaporant source is sufficient to insure uniform deposition, the thickness of the SiO layer

can be determined with reasonable accuracy by the following calculation:

$$d = \frac{m_f}{\rho A} = \frac{M_i N_f'}{\rho A \; N_i'} \qquad (24)$$

where

d: thickness of SiO layer

M_i: mass of initial SiO sample

m_f: mass of SiO deposited on substrate

A: area of SiO layer = 2.37 cm^2

N_i': count rate of initial sample corrected for coincidence loss

N_f': count rate of evaporated SiO layer corrected for decay time

ρ: density of SiO 2.15 g/cm^3

Self absorption and G.M. tube window losses should introduce little error since the emitted β energy is high. The geometry correction is minimized by counting both the initial sample and the evaporated layer at approximately 8 cm from the G.M. tube window. A calculation of relative solid angles subtended at the G.M. tube by the initial point source and the evaporated disk shows a difference of 0.3%. Additional error is introduced here by the uncertainty concerning the density of thin layers of evaporated materials. This density can be as much as 20% lower than the bulk density.

IV. DATA

Figures 14-a, b, and c are normalized curves which show the fractional currents measured in the top and bottom aluminum layers as a function of proton energy in keV. The currents are measured by the procedure outlined in Section III-E with readings taken at two kilovolt intervals and repeated on several successive days to provide an average. Resistance monitoring showed no change in the insulating layer of SiO for the targets for which data is included. Each had an initial resistance of approximately 1 megohm between the aluminum layers, and the measured thickness of the silicon monoxide layer for each was near the optimum of 75 Å. After exposure to the proton beam, the target surfaces were inspected by optical magnification to ensure that no increase in thickness of the top layer had occurred as a result of pump oil dissociation and deposit.

In the energy region below 2 keV a small negative current is observed consistently in the bottom collector. The magnitude of this current is typically about 1% of the total beam current and is attributed to secondary electrons originating in the top aluminum layer and passing through the target to the bottom collector.

Figure 15 shows the proton charge transmission probability as a function of energy. These curves are derived from the proton current data in Figures 14-a, b, and c by the method described in Section II-B. Vertical dashed lines are drawn from each curve to indicate the energy at which 50% of the incident protons are transmitted through the respective aluminum thickness.

Figure 16 is a curve of aluminum thickness as a function of energy for penetration of 50% of the incident proton charge.

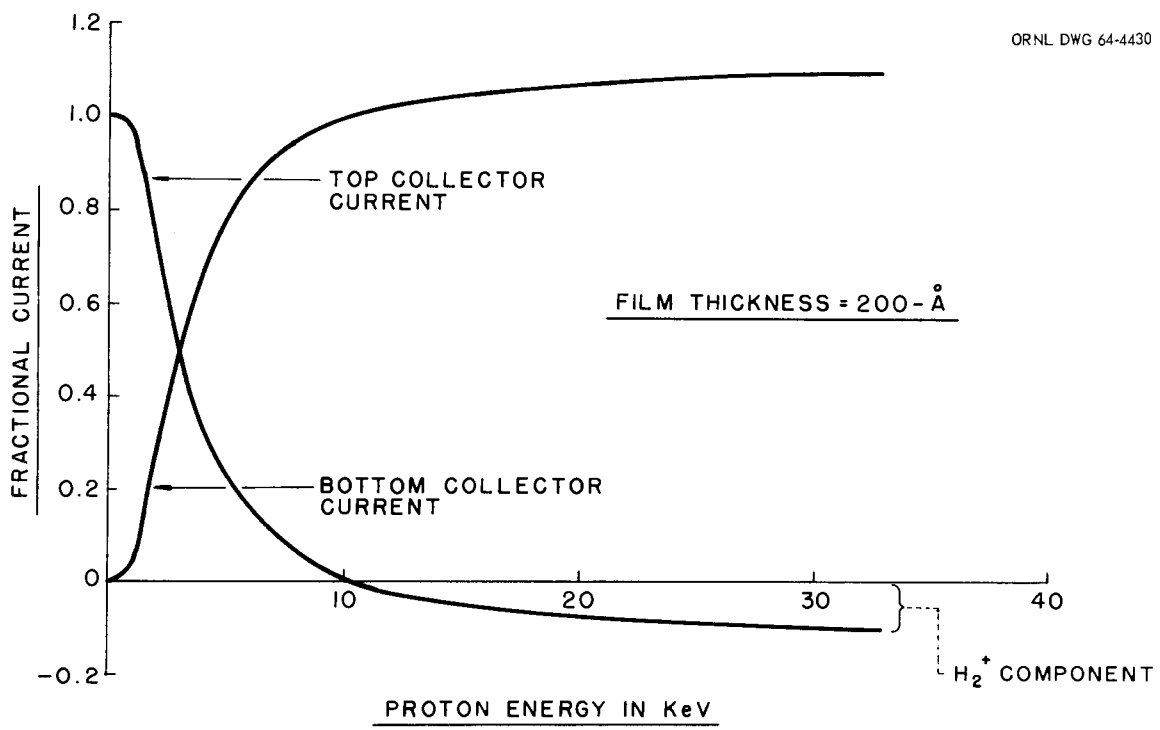

Fig. 14a. Fractional Current Distribution in the Aluminum Layers versus Proton Energy for Aluminum Thickness 200 Å.

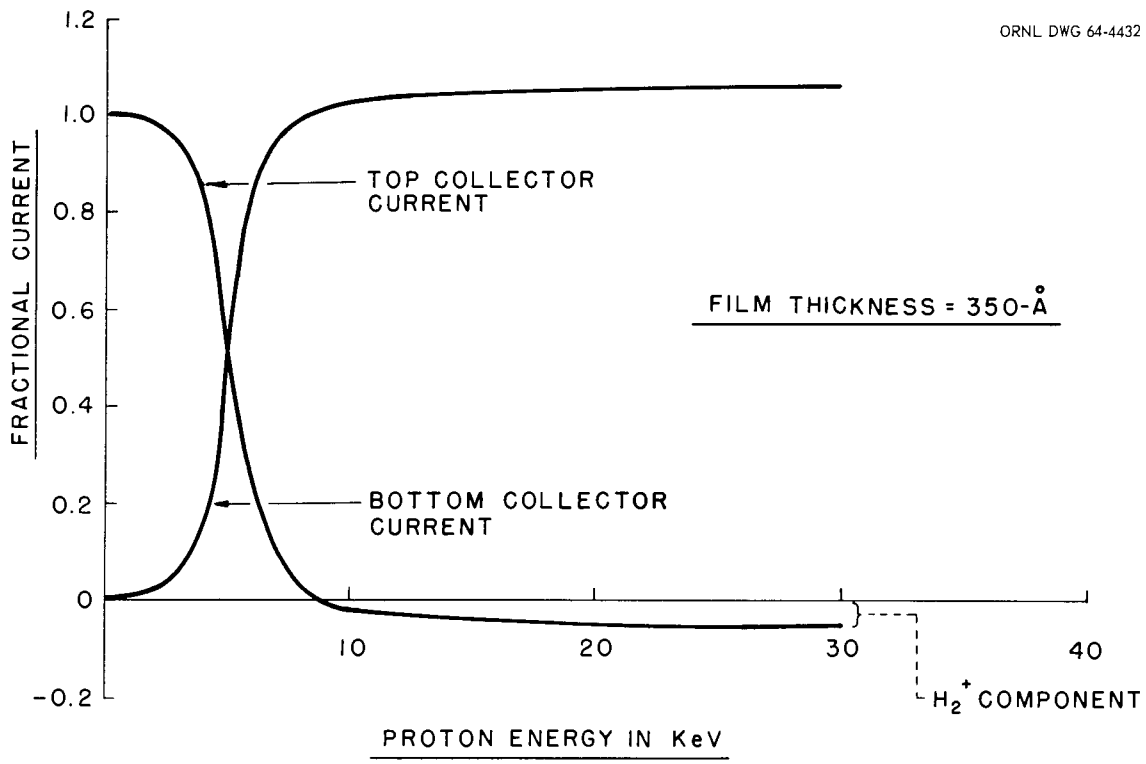

Fig. 14b. Fractional Current Distribution in the Aluminum Layers versus Proton Energy for Aluminum Thicknesses 350 Å.

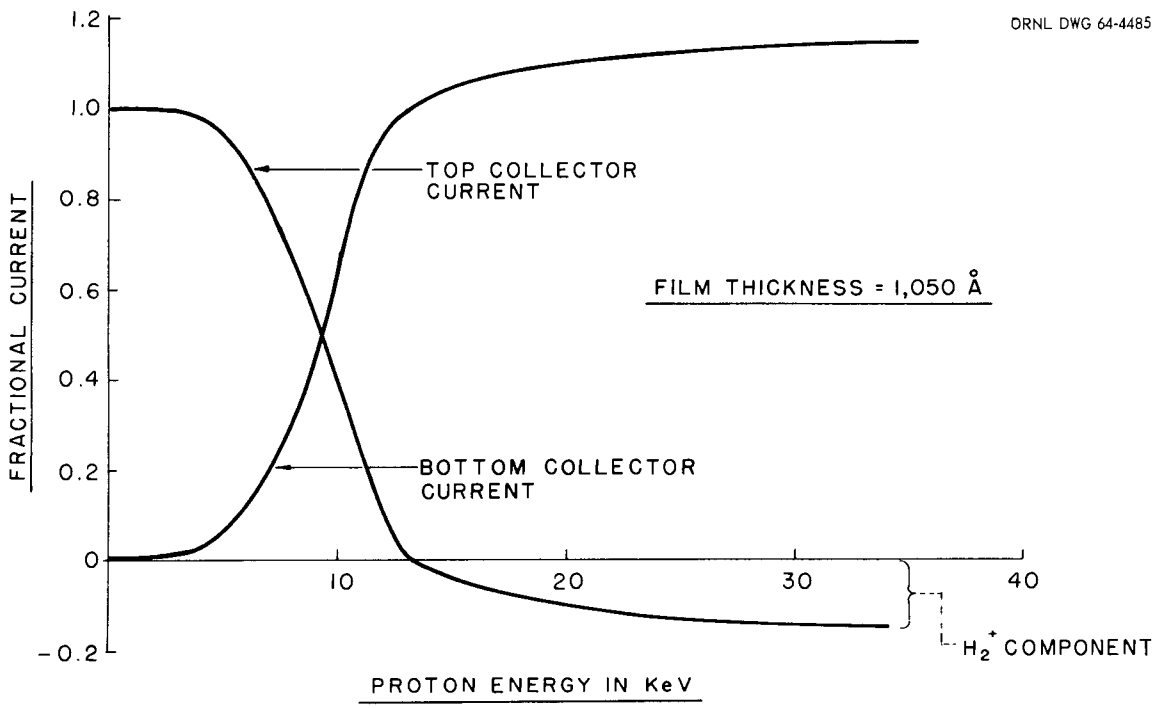

Fig. 14c. Fractional Current Distribution in the Aluminum Layers versus Proton Energy for Aluminum Thicknesses 1,050 Å.

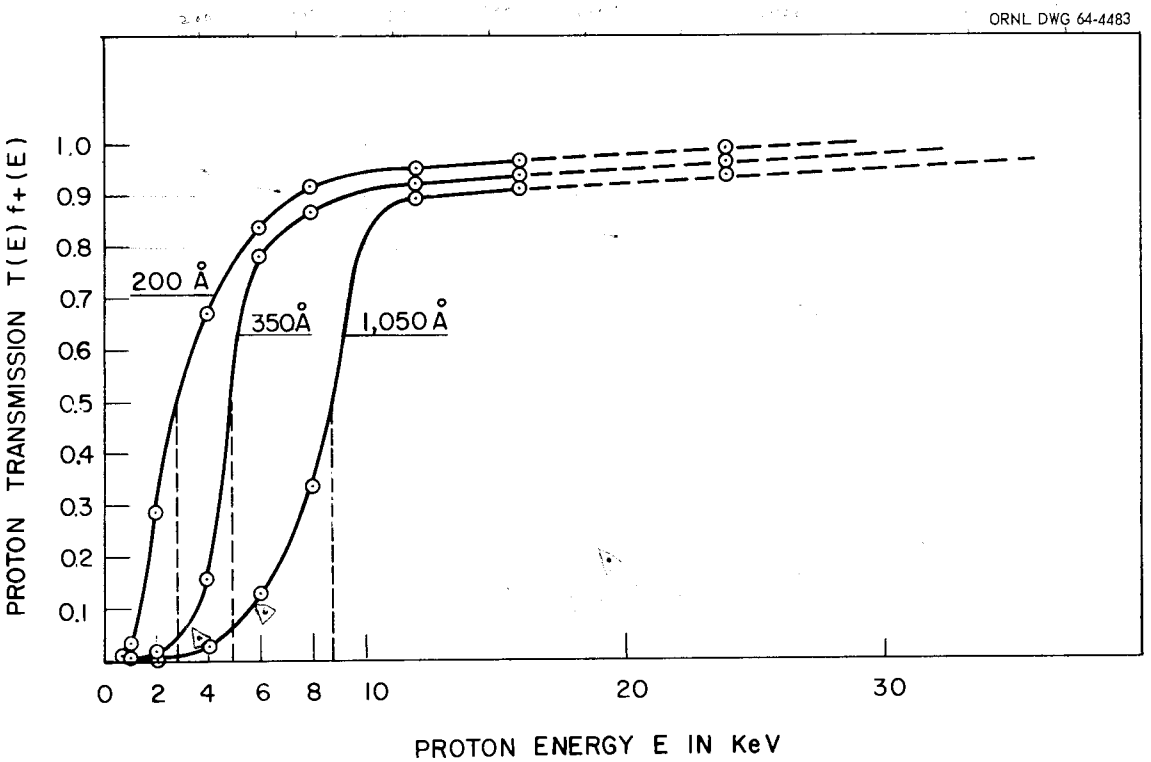

Fig. 15. Proton Transmission as a Function of Energy for Several Aluminum Thicknesses.

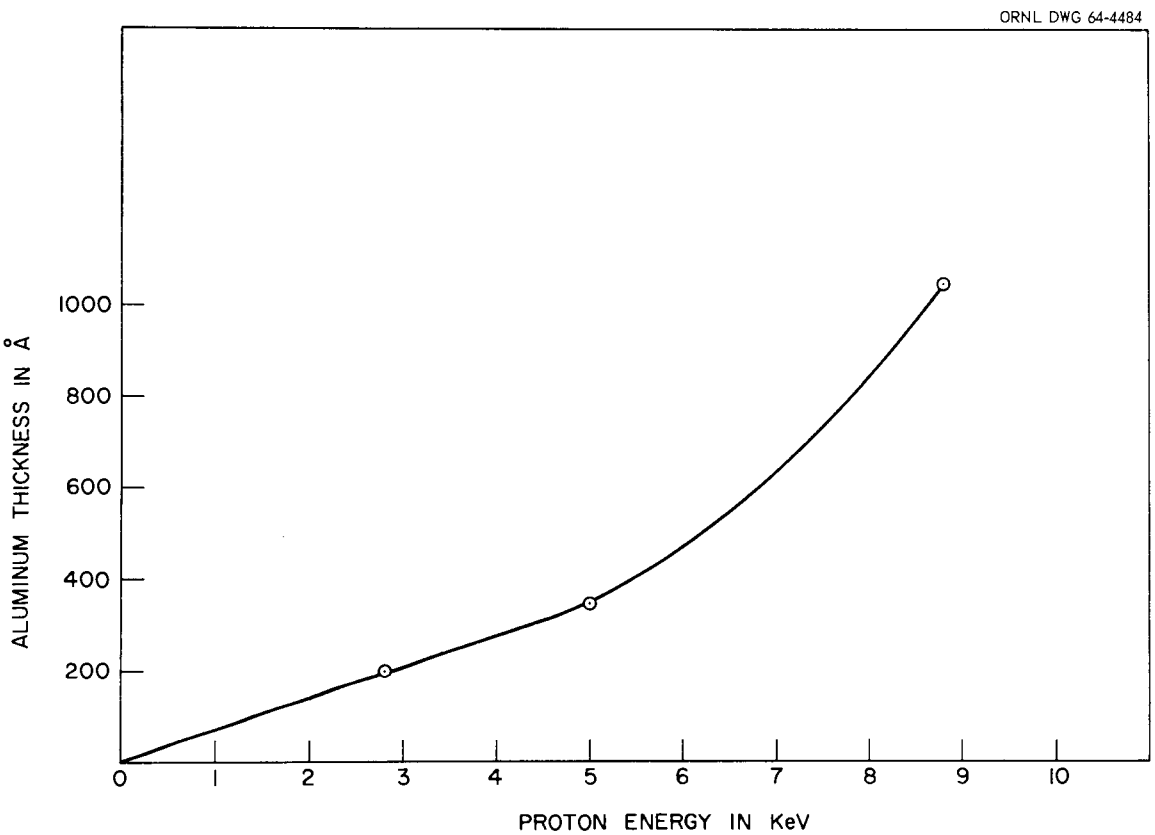

Fig. 16. Aluminum Thickness as a Function of Energy for 50% Proton Transmission.

V. RESULTS

Figure 17 is a comparison of our range-of-charge curve with range theory and the available experimental data for particle ranges. The Lindhard-Scharff curve is calculated using the range-energy formula derived in Section II-A. The stopping power theory is based on an absolute range of protons and does not consider charge exchange phenomena likely to be significant in any experimental determination of ranges. The Hines curve is a conversion to protons of range-energy data measured for deuterons in aluminum. The energy loss due to ionization per unit path length, dE/dx, is the same for deuterons and protons of the same velocity. But a deuteron has twice the energy of a proton at the same velocity. Thus the range of protons at half the energy of deuterons should be half the range measured for deuterons. Hines' data measures the transmission of 50% of the incident beam.[23]

Young's curve presents data for protons in aluminum and is a measure of range for protons at the maximum beam energy. His data is fitted by the expression[24]

$$R(\mathring{A}) = 200\ E(\mathrm{keV})^{0.83} \tag{25}$$

The data presented in this work is lower than that of Hines and Young at low energy because they measured the particle range and we measured the product of this and the probability that the particle

---

[23] R. L. Hines, Phys. Rev. 132, 701-706 (1963).

[24] J. R. Young, J. Appl. Phys. 27, 1-4 (1956).

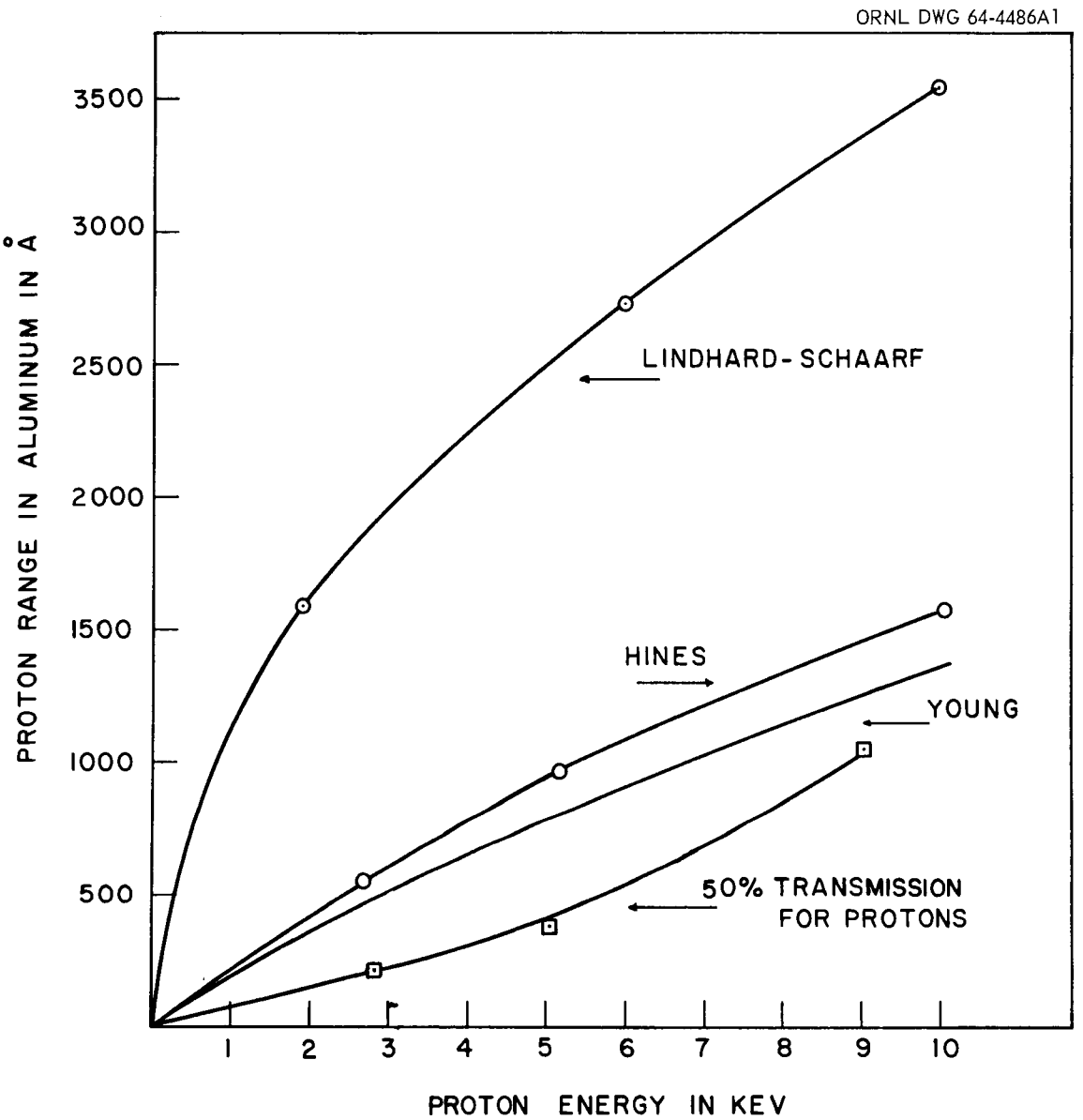

Fig. 17. Comparison of Theoretical and Experimental Range-Energy Curves.

has a charge + 1 as it leaves the top layer. This probability is less than one at low energies. However, this data does tend to approach that of Hines and Young above about 10 keV, as would be expected since the charge transfer cross-section decreases above this energy.

VI. REVIEW AND CONCLUSIONS

The results shown here demonstrate the applicability of this method to range-energy studies for low energy charged particles in conducting solids. The data accumulated to date is perhaps insufficient to establish a new range-of-charge versus energy measurement for protons in aluminum. Of sixty evaporated targets only three yielded current-energy curves with sufficient reproducibility to permit analysis. The thickness of the silicon monoxide insulating layer is a critical limiting factor, and the nonuniformity of evaporated layers at this thickness resulted frequently in contact shorts between the aluminum layers. Another frequent cause of target failure was radiation damage or heat damage to the silicon monoxide layer resulting in irreparable resistance loss. Several targets which initially yielded good results did not perform in a reproducible manner, indicating a deposition of hydro-carbon contaminants from the vacuum system, and these were discarded.

This work is being continued by the staff of the Radiation Physics Section of the ORNL Health Physics Division. More sophisticated evaporation techniques are being developed to perfect the target fabrication procedure. A rotary turbine pumping system has been installed and already indicates a reduction in hydro-carbon contamination. Several suggestions have also been made to improve the ion purity of the incident beam, and subsequent investigations may utilize deflection analysis techniques to remove the H_2^+ from the proton beam.

BIBLIOGRAPHY

Allan, H. R. and Sarma, N., "An Improved Design of Radio-Frequency Ion Source," J. Sci. Instr. 33, 447-448 (1956).

Allison, S. K. and Norbeck, E., "Simplified Radio-Frequency Ion Source," Rev. Sci. Instr. 27, 285-288 (1956).

Allison, S. K. and Warshaw, S. D., "Passage of Heavy Particles Through Matter," Rev. Mod. Phys. 25, 779-817 (1953).

Arakawa, E.T., "Ion Extraction Studies for a Radio-Frequency Ion Source," Thesis, Louisiana State University (1951).

Bethe, H. A. and Ashkin, J., Experimental Nuclear Physics, E. Segre, Ed. (John Wiley and Sons, Inc., New York) Vol. 1, ch. 2 (1953). A comprehensive review of the energy loss process.

Bichsel, H., "Experimental Range of Protons in Aluminum" Phys. Rev. 112, 182-185 (1958).

Billington, D. S., and Crawford, J. H., Radiation Damage in Solids, (Princeton University Press) (1961).

Bohr, N., Kgl. Danske Videnskab. Selskab Mat. Fys. Medd. 18, No. 8, (1948).

Brown, R. E. and Jarmie, N., Index and Annotated Bibliography of Range and Stopping Cross Section Data, Compl. LA-2156 (1958).

Domeij, B., Brown, F., Davies, J. A., Piercy, G. R. and Kornelsen, E. V. "Anomalous Penetration of Heavy Ions of KeV Energies in Mono-Crystalline Tungsten," Phys. Rev. Letters 12, 363-365 (1964).

Emerson, L. C., Arakawa, E. T., Ritchie, R. H., and Birkhoff, R. D., "Emission Spectra of Electron Irradiated Metal Foils," ORNL-3450 (1963).

Eubank, H. P., Peck, R. A., and Truell, R., "Operating Characteristics of a High Yield Rf Ion Source," Rev. Sci. Instr. 25, 989-995 (1954).

Hall, T., "Ratio of Cross Sections for Electron Capture and Electron Loss by Proton Beams in Metals," Phys. Rev. 79, 504-512 (1950).

Harvey, G. B., Ann. Rev. Nucl. Sci. 10, 235 (1960).

Hines, R. L., "Ranges of 5 to 27-keV Deuterons in Aluminum, Copper and Gold," Phys. Rev. 132, 701-706 (1963).

Jackson, J. D. and Schiff, H., "Electron Capture by Protons Passing Through Hydrogen," Phys. Rev. 89, 359-365 (1953).

Kahn, D., "The Energy Loss of Protons in Metallic Foils and Mica," Phys. Rev. 90, 503-509 (1953).

Knipp, J. and Teller, E., "On the Energy Loss of Heavy Ions," Phys. Rev. 59, 659-669 (1941).

Lindhard, J., Kgl. Danske Videnskab. Selskab Mat. Fys. Medd 28, No. 8 (1954).

Lindhard, J. and Scharff, M., "Energy Dissipation by Ions in the keV Region," Phys. Rev. 124, 128-130 (1961).

Massey, H.S.W. and Burhop, E.H.S., Electronic and Ionic Impact Phenomena, (Oxford), (1952).

Meyerhofer, D. and Ochs, S. A., "Current Flow in Very Thin Films of Al_2O_3 and BeO," J. Appl. Phys. 34, 2535-2543 (1963).

Moak, C. D., Reese, H., and Good, W. M., "Design and Operation of a Radio-Frequency Ion Source for Particle Accelerators," Nucleonics 9, No. 3, 18-23 (1951).

Parkinson, D. B., Herb, R. G., Bellamy, J. C., and Hudson, C. M., "The Range of Protons in Aluminum and Air," Phys. Rev. 52, 75-79 (1937).

Person, S., Hutchinson, F., and Marvin, D., "Range of Low-Energy Protons in Protein," Rad. Res. 18 397-406 (1963).

Phillips, J. A., "The Energy Loss of Low Energy Protons in Some Gasses," Phys. Rev. 90, 532-537 (1953).

Phillips, J. A., "Charge Equilibrium Ratios for Hydrogen Ions from Solids," Phys. Rev. 97, 404-410 (1955).

Powers, D. and Whaling, W., "Range of Heavy Ions in Solids," Phys. Rev. 126, 61-69 (1962).

Reynolds, H. K., Dunbar, D.N.F., Wenzel, W. A., and Whaling, W., "The Stopping Cross Section of Gasses for Protons, 30-600 KeV," Phys. Rev. 92, 742-748 (1953).

Rich, M. and Madey, R., "Range Energy Tables," UCRL-2301 (1954).

Seitz, F., Koehler, J. S., Solid State Physics, Vol. 2, 305 (1955).

Sternheimer, R. M., "Range-Energy Relations for Protons in Be, C, Al, Cu, Pb, and Air," Phys. Rev. 115, 137-142 (1959).

Sternheimer, R. M., "Range-Energy Relations for Protons in Various Substances," Phys. Rev. 118, 1045-1048 (1960).

Taylor, A. E., "Range-Energy Relations" Rep. on Prog. in Phys. 15, 49-67 (1952).

Van Wijngaarden, A. and Duckworth, H. E., "Energy Loss in Condensed Matter of H^1 and He^4 in the Energy Range 4 eV to 30 keV," Can. J. Phys. 40, 1749-1764 (1962).

Ward, O. G., "Radiofrequency Ion Sources," Helv. Phys. Acta 23, 27 (1950).

Warshaw, S. D., "Stopping Power for Protons in General Metals," Phys. Rev. 76, 1759-1765 (1949).

Wilcox, H. A., "Experimental Determination of Rate of Energy Loss for Slow H^1, H^2, He^4, Li^6 Nuclei and Au and Al," Phys. Rev. 74, 1743 (1948).

Whaling, W., Handbuch der Physik, 34, 192 (1958). "The Energy Loss of Charged Particles in Matter."

Young, J. R., "Penetration of Electrons and Ions in Aluminum," J. Appl. Phys. 27, 1-4 (1956).

Zumwalt, L. R., "Absolute Beta Counting Using End Window GM Counters and Experimental Data on Beta-Particle Scattering Effects," AECV-567 (1950).

ORNL-3702
UC-34 — Physics
TID-4500 (37th ed.)

INTERNAL DISTRIBUTION

1. Biology Library
2-4. Central Research Library
5. Reactor Division Library
6-7. ORNL — Y-12 Technical Library Document Reference Section
8-57. Laboratory Records Department
58. Laboratory Records, ORNL R.C.
59-78. E. T. Arakawa
79. R. Baldock
80. C. Barnett
81-105. R. D. Birkhoff
106. R. H. Boyett
107. H. R. Brashear
108. L. C. Emerson
109. A. C. England
110. R. B. Evans III
111. B. E. Foster
112-113. W. Garber
114-115. J. A. Harter
116. F. F. Haywood
117. H. H. Hubbell, Jr.
118. G. S. Hurst
119. D. R. Johnson
120. W. H. Jordan
121. C. E. Larson
122. H. G. MacPherson
123. A. Meyer
124. K. Z. Morgan
125-139. M. Y. Nakai
140-141. D. Pittman
142-146. R. H. Ritchie
147. M. J. Skinner
148. J. L. Stanford
149. J. H. Thorngate
150. J. E. Turner
151. A. M. Weinberg
152. J. C. Frye (consultant)
153. J. B. Hursh (consultant)
154. J. L. Magee (consultant)
155. E. P. Odum (consultant)
156. H. O. Wyckoff (consultant)

EXTERNAL DISTRIBUTION

157. Jens Lindhart, Institute of Physics, University of Aarhus, Aarhus, Denmark
158. Robert Wood, Division of Biology and Medicine, AEC, Washington, D.C.
159. Nathaniel Barr, Division of Biology and Medicine, AEC, Washington, D.C.
160. J. A. Lough, Division of Biology and Medicine, AEC, Washington, D.C.
161. J. R. Young, General Electric Research Laboratory, Schenectady, New York
162. R. L. Hines, Northwestern University, Evanston, Illinois
163-172. A. K. Roecklein, Montgomery Junior College, Tekoma Park, Maryland
173. Arie Van Wijngaarden, Department of Physics, Assumption University, Windsor, Ontario
174. H. E. Duckworth, Department of Physics, McMaster University, Hamilton, Ontario
175. V. B. Bhanot, Physics Department, Panjab University, Chandigarh-3, India
176. Research and Development Division, AEC, ORO
177-821. Given distribution as shown in TID-4500 (37th ed.) under Physics category (75 copies — CFSTI)